CrossMark

Structural Controls on Groundwater Flow in Basement Terrains: Geophysical, Remote Sensing, and Field Investigations in Sinai

Lamees Mohamed[1,2] · Mohamed Sultan[1] · Mohamed Ahmed[1,3] ·
Abotalib Zaki[1] · William Sauck[1] · Farouk Soliman[3] ·
Eugene Yan[4] · Racha Elkadiri[1] · Abdou Abouelmagd[3,5]

Abstract An integrated [very low frequency (VLF) electromagnetic, magnetic, remote sensing, field, and geographic information system (GIS)] study was conducted over the basement complex in southern Sinai (Feiran watershed) for a better understanding of the structural controls on the groundwater flow. The increase in satellite-based radar backscattering values following a large precipitation event (34 mm on 17–18 January 2010) was used to identify water-bearing features, here interpreted as preferred pathways for surface water infiltration. Findings include: (1) spatial analysis in a GIS environment revealed that the distribution of the water-bearing features (conductive features) corresponds to that of fractures, faults, shear zones, dike swarms, and wadi networks; (2) using VLF (43 profiles), magnetic (7 profiles) techniques, and field observations, the majority (85 %) of the investigated conductive features were determined to be preferred pathways for groundwater flow; (3) northwest–southeast- to north–south-trending conductive features that intersect the groundwater flow (southeast to northwest) at low angles capture groundwater flow, whereas northeast–southwest to east–west features that intersect the flow at high angles impound groundwater upstream and could provide potential productive well locations; and (4) similar findings are observed in central Sinai: east–west-trending dextral shear zones (Themed and Sinai Hinge Belt) impede south to north groundwater flow as evidenced by the significant drop in hydraulic head (from 467 to 248 m above mean sea level) across shear zones and by reorientation of regional flow (south–north to

✉ Mohamed Sultan
mohamed.sultan@wmich.edu

1 Department of Geosciences, Western Michigan University, 1903 West Michigan Avenue, Kalamazoo, MI 49008, USA

2 Department of Geology, Mansoura University, Mansoura 35516, Egypt

3 Department of Geology, Suez Canal University, Ismailia 41522, Egypt

4 Environmental Science Division, Argonne National Laboratory, Argonne, IL 60439, USA

5 Earth System Observation and Modeling, Water Desalination and Reuse Center, King Abdullah University of Science and Technology (KAUST), Thuwal 23955-6900, Kingdom of Saudi Arabia

southwest–northeast). The adopted integrated methodologies could be readily applied to similar highly fractured basement arid terrains elsewhere.

Keywords Sinai · Groundwater flow · Very low frequency · Magnetic · Radar backscattering · Remote sensing

1 Introduction

Demand for freshwater supplies in arid and hyper-arid countries worldwide is on the rise because of increasing populations and the paucity of available water resources. This problem is exemplified in the Saharan African countries. Egypt, as is the case with the remaining Saharan African countries, is suffering from scarcity of modern precipitation and increasing population (20 million people in 1950; 83 million in 2014) (CAPMAS 2014). To meet its rising demands for freshwater resources, Egypt heavily relies on Nile River waters that originate as allochthonous precipitation over the Ethiopian highlands and equatorial Africa, and on fossil autochthonous precipitation that recharged its fossil aquifers [e.g., Nubian Sandstone Aquifer System (NSAS)] during previous wet climatic periods (Thorweihe 1982; Sultan et al. 1997). Given the unsustainable nature of the NSAS and the ongoing disputes between the countries (i.e., Egypt and Ethiopia) on the Nile River on water allocations, alternative renewable water resources should be identified.

The Sinai Peninsula (Fig. 1a) is one of the most promising regions for the development of alternative water resources in Egypt given the relatively high amounts of precipitation. Examination of the three-hourly precipitation data from the Tropical Rainfall Measuring Mission (TRMM; 1998–2013; 3B42v7A) shows that the average annual precipitation over the Western Desert, Eastern Desert, and Sinai is 9, 13, and 70 mm, respectively (Fig. 1b). Rainfall over the mountainous [e.g., Saint Catherine mountain; elevation 2641 m above mean sea level (AMSL); Fig. 1b] basement complex in southern Sinai is channeled as surface runoff in wadi networks and as subsurface groundwater flow in wadi fills and fractured basement rocks (Fig. 1a). Favorable settings for hosting and channeling groundwater within the basement complex include areas of enhanced porosity where faults, fractures, and/or shear zones (meters to tens of meters wide) intersect (Goddard and Evans 1995; Blenkinsop and Kadzviti 2006; Sultan et al. 2008).

In this paper, we develop and apply integrated [geophysics, remote sensing, geographic information system (GIS), and field observations] cost-effective methodologies for a better understanding of the spatial distribution and role of structural elements (e.g., shear zones, faults, fractures, and dikes) in channeling, impeding, and redirecting groundwater flow in the Feiran watershed (width 22 km; length 72 km; area 1770 km^2) in southern Sinai (Fig. 1a). Our findings were then applied in central Sinai to gain insights into the structural control on the groundwater flow across the entire Sinai Peninsula. The adopted approach entails delineating structural elements in the study area, identifying the structures that are preferred pathways for surface water infiltration, and testing whether the identified structures are preferred pathways for groundwater flow using geophysical and field data. Deciphering groundwater flow in sedimentary aquifer systems is straightforward once head data become available; this is not the case in fractured basement aquifer systems given their heterogeneity in hydraulic properties (e.g., porosity and permeability), making

Fig. 1 a Location map showing the distribution of Precambrian outcrops and overlying Phanerozoic rock units in Sinai, Feiran watershed (*red polygon*), hydraulic head data (*blue lines*) and regional groundwater flow (*black arrows*) for the NSAS in central Sinai extracted from 25 wells (*green circles*; Rosenthal et al. 2007), and three main shear zones (*purple lines*) (Bosworth and McClay 2001; Moustafa et al. 2013). *Inset* shows the regional distribution of the Arabian Nubian Shield outcrops. **b** Average annual precipitation extracted from 3-hourly TRMM 3B42v7A data acquired (1998–2013) over Egypt and surrounding countries. **c** Locations of VLF and magnetic profiles acquired in 2011, 2012, and 2013

groundwater flow only possible along preferred pathways. We provide straightforward, practical, and cost-effective methodologies to map the preferred groundwater flow pathways in basement terrains. This study could potentially have regional and global implications as well.

2 Geologic, Hydrogeologic, and Climatic Settings

The exposed Proterozoic crystalline rocks in the southern Sinai Peninsula (Fig. 1a) together with those in the northern Eastern Desert of Egypt represent the northwestern extension of the Arabian–Nubian Shield (ANS; inset Fig. 1a). The earlier phases (950–650 Ma) of evolution of the ANS in Sinai involved the accretion of island arcs and closure of interleaving oceanic basins that gave way to an intraplate extensional phase, and by 450 Ma, the terrain transitioned to a stable cratonic phase (Garfunkel 1999). The extensional phase was characterized by bimodal mafic (basalt and basaltic andesite) and felsic (dacite, rhyodacite, and rhyolite) dike swarms (Stern et al. 1984, 1988; Eyal and Eyal

1987; Friz-Topfer 1991). The main rock units encountered in southern Sinai (Fig. 1a) are largely (70 % of area is outcrop) composed of syn- and post-orogenic granitoids with additional metagabbros, metadiorites, metavolcanics, metasediments, and gneissic and migmatitic rocks of variable compositions (Shimron 1973; Eyal 1975; Bartov et al. 1979; Issar and Gilad 1982).

The complex and prolonged tectono-magmatic history of the southern Sinai gave rise to various generations and modes of magmatic and volcanic activities and a wide range of structural elements and styles of deformation. The study area is highly dissected by numerous brittle faults and shear systems; the most prominent of these systems are northwest-trending sinistral faults and shear systems that are dissected by northeast-trending dextral faults and shear zones. The sinistral faults are here interpreted to be post-accretionary Najd faults of late Precambrian age. The Najd shear system extends over 1200 km in a northwest–southeast direction in the Arabian Shield, with an average width of ∼300 km (Agar 1987), and aligns with faults in the south Yemen coast (Brown and Coleman 1972), making a potential total length in excess of 2000 km (Moore 1979). Using a pre-Red Sea rift reconstruction, together with field, geochemical, and geochronological data, Sultan et al. (1988, 1992, 1993) mapped the extension of the Najd shear system of the Arabian Shield into the Central Eastern Desert of Egypt, bringing the total length of the Najd system in the ANS to 2300 km. Along the zone occupied by the Najd system in the ANS, brittle and ductile styles of deformation prevail, superimpose on, and obliterate earlier accretionary tectonic features (Sultan et al. 1988). A major northwest-trending Najd shear zone (the Rihba shear zone: length 50 km; width 200 m; Fig. 1a) that extends in our study area was reported (Moustafa 1997; Bosworth and McClay 2001; Younes and McClay 2002; Sultan et al. 2012).

The origin of the dextral fault system is less constrained. It could represent the conjugate fault set to the main northwest-trending Najd shear system as commonly observed in the ANS (Moore 1979; Greiling et al. 1994; Johnson and Woldehaimanot 2003; Shalaby 2010). Alternatively, the dextral fault system could be much younger in age. The sinistral slip (post-Early Miocene to Recent) on the Dead Sea Transform and associated drag on the eastern edges of preexisting east–west- to east-northeast–west-southwest-oriented faults could have resulted in simple dextral wrenching (Moustafa and Khalil 1994). Also, a transtensional origin for these dextral faults was proposed, where the throw along the Gulf of Suez rift-related northwest–southeast-oriented faults could have caused Late Oligocene to Early Miocene divergent dextral wrenching along preexisting faults (Moustafa and Khalil 1994; Moustafa 1997; Younes and McClay 2002).

The basement complex of southern Sinai is dissected by numerous vertical to subvertical dike swarms (length 0.1–15 km; width 0.5–20 m) of mafic, intermediate, and felsic compositions (Stern et al. 1988; Iacumin et al. 1998). Dike swarms in the study area are classified into three main groups based on their age of emplacement: (1) metamorphosed syn-tectonic dikes (age 800–650 Ma; Eyal and Eyal 1987); (2) widely distributed, unmetamorphosed, post-orogenic dikes (591–459 Ma) of extensional, late Pan-African origin (Stern et al. 1984, 1988; Iacumin et al. 1998); and (3) Neogene dikes (30–12 Ma) related to the extensional forces associated with the Red Sea Rift system (Meneisy 1990). The first two groups are mafic, intermediate, and felsic in composition, whereas the Neogene dikes have basaltic compositions (El-Sayed 2003).

Precipitation in the study area is largely controlled by orographic effects; moist air masses are forced to higher altitudes where condensation occurs, causing rainfall or snow deposition. The dense networks of valleys collect precipitation over extensive areas and channel it downstream through the main valleys causing flash floods. It has been

demonstrated that in areas with similar geologic, hydrologic, and climatic settings in the Eastern Desert of Egypt, precipitation over the basement complex highlands is channeled downstream as surface runoff in valley networks and as groundwater flow in the alluvial sediments underlying these valleys, in fractured basement, and in down-dropped sedimentary units within the basement complex (Sultan et al. 2007, 2008, 2011; Amer et al. 2013). We envision a similar conceptual model for the Feiran watershed. The Feiran watershed channels precipitation over the highlands [e.g., Saint Catherine mountain and Moses mountain (elevation 2285 m AMSL); Fig. 1a] toward the Gulf of Suez coastal plain. Fractured basement and alluvial aquifers prevail throughout the Feiran watershed. Only in and proximal to the coastal plain do we observe rift-related, aquifer systems (e.g., El Qaa aquifer system) within down-dropped blocks (Ahmed et al. 2013). In these areas, the alluvial aquifers are often floored by Miocene to Post-Miocene sandstone (i.e., Nukhul) and Lower Cretaceous sandstone (i.e., NSAS) aquifers.

3 Methodology and Findings

We adopted an integrated (remote sensing, field, geophysics, and GIS) six-step methodology that involved the following: (1) compilation of a multitude of relevant data sets in a GIS environment for visualization and analyses; (2) identification of precipitation events from TRMM for which radar imagery is available prior to and after the event; (3) identification of water-bearing areas that witnessed an increase in the backscattering coefficient values extracted from radar [Environmental Satellite's (Envisat's) Advanced Synthetic Aperture Radar (ASAR)] images; (4) identification of the nature (e.g., faults, shear zones, dikes, or wadis) of the water-bearing features and mapping their spatial distribution using visible and near-infrared (VNIR) remotely acquired data sets (Landsat 7 and Google Earth Digital Globe Imagery); (5) acquisition of field and geophysical data [magnetic, very low frequency (VLF) electromagnetic] to test whether the water-bearing features and their postulated extension in wadis represent preferred pathways for groundwater flow within the study area; and (6) investigation of the impact of water-bearing features on groundwater flow in the Feiran watershed and the regional applications of our findings across the Sinai Peninsula.

3.1 Construction of a GIS Database

The Sinai GIS database incorporates co-registered digital mosaics generated from relevant data sets with a unified projection (type: UTM Zone 36 N, datum: WGS-1984). Regional data sets for Sinai are grouped into the following categories: base maps, geophysics, topography, remote sensing, hydrology, and geology. Each category contains a set of digital layers. These digital products include: (1) geologic map and data sets for geologic units and structures within the Feiran watershed (scale 1:500,000) (Klitzsch et al. 1987); (2) digital elevation models (DEMs; spatial resolution: 30 m) extracted from Advanced Spaceborne Thermal Emission and Reflection Radiometer (ASTER) data; (3) watershed boundary and stream network distribution extracted from the generated DEMs using the topographic parametrization (TOPAZ) technique (Martz and Garbrecht 2002); (4) two Landsat 7 thematic mapper (TM) scenes (scene ID: LE71740402000254SGS00, L71175040_04020090419; spatial resolution: 30 m); (5) false-color mosaic of VNIR TM band images (blue: 7; green: 4; red: 2); (6) false-color mosaic of VNIR TM band ratio color

composite images (blue: 5/4 × 3/4; green: 5/1; red: 5/7) that are sensitive to the content of Fe-bearing aluminosilicates, spectrally opaque, and hydroxyl-bearing or carbonate-bearing minerals, respectively (Sultan et al. 1987, 1988); (7) Google Earth images (spatial resolution 0.65–2.62 m); (8) distribution of faults, shear zones, felsic, and mafic dikes extracted from geologic maps, Google Earth, false-color TM, and band ratio color composite images; (9) daily precipitation data (for years 2002 through 2012) extracted from 3-hourly TRMM data; (10) backscatter coefficient scenes generated from four ASAR C-band (central wavelength: 8.5 cm; spatial resolution: 30 m) scenes (ID: ASA_IMS_IPTDPA20091111, acquisition date: 11 November 2009; ID: ASA_IMS_1PTDPA20091127, acquisition date: 27 November 2009; ID: ASA_IMS_1PTDPA2010120, acquisition date: 20 January 2010, and ID: ASA_IMS_1PTDPA20100205, acquisition date: 5 February 2010); (11) two backscatter coefficient mosaics: the first (mosaic I) generated from the two scenes pre-dating the precipitation event (17–18 January 2010) and the second (mosaic II) from those following the precipitation event; (12) a false-color composite (red: $\left(\frac{\text{mosaic II–mosaic I}}{\text{mosaic II+mosaic I}}\right)$, blue and green: mosaic I) ASAR normalized difference image; (13) 43 color-coded, Fraser-filtered, VLF tilt-angle profiles; (14) 7 color-coded magnetic profiles; (15) published well data (location, name, and depth to water table) for 52 wells (Aggour 2007); and (16) additional well locations (250 wells) that were extracted from Google Earth images by identifying farms and neighboring open wells that were dug for irrigation purposes.

3.2 Identification of Precipitation Events for Which Radar Imagery is Available

TRMM is a joint mission between Japan and USA launched in 1997. TRMM provides global (50°N–50°S) data on rainfall using microwave and VNIR sensors (Kummerow et al. 1998; Huffman et al. 2007). Instantaneous rainfall estimates are obtained every 3 h with a 0.25° × 0.25° footprint and continuous coverage from 1998 to 2015. In this step, TRMM data (version 3B42.007A) were used to examine the amplitude and the spatial and temporal distributions of rain events over the Feiran watershed. Examination of the TRMM-derived daily rainfall time series shows 12 rain events ranging in amplitude from 15.3 to 34 mm for the time period January 1999 to December 2012. The rain event that occurred on 17–18 January 2010, was selected for radar-based investigations for two main reasons: it is during these 2 days that the highest amount of precipitation (34 mm) among the recorded 12 events was reported, and it is the only event for which radar scenes were acquired only days before and after the event over the Feiran watershed. Next, we show how these two radar scenes were used to examine the change in soil moisture within the Feiran watershed.

3.3 Identification of Water-Bearing Features from Temporal Radar Imagery

One of the main payloads on the Envisat mission [launched by European Space Agency (ESA) on 1 March 2002] is the ASAR sensor. Four ASAR scenes were collected and processed to extract the backscatter coefficient values. Routine processing steps including the orbital correction, multi-looking, co-registration, filtering, geocoding, and radiometric calibration were applied to the ASAR scenes. Two of the selected images (acquisition date: 11 and 27 November 2009) were acquired before a TRMM-derived precipitation event on 17–18 January 2010; the other two scenes were acquired (20 January and 5 February 2010)

after the event. Extracted backscatter values are a function of the dielectric constant, which is largely controlled by the moisture content of the imaged material; the larger the moisture content, the greater the dielectric constant, and vice versa (Wang et al. 2004, 2011). To examine the changes in moisture content across the Feiran watershed, we first generated two mosaics from the individual backscatter images, one from scenes acquired before the precipitation event (mosaic I) and another from scenes acquired after the event (mosaic II). A normalized difference image was first generated by subtracting mosaic I from mosaic II and dividing the difference image by the sum of the two mosaics. The reciprocal of this image is the Normalized Radar Backscatter Soil Moisture Index (NBMI) (Shoshany et al. 2000), a ratio that maximizes changes in the backscatter coefficient related to soil moisture variability and minimizes changes related to other effects (Lu and Meyer 2002; Shoshany et al. 2000; Wagner and Scipal 2000; Wickel et al. 2001).

A color composite image was then generated from two co-registered mosaics, the normalized difference image (assigned the red color), and mosaic I (assigned the blue and green colors) to display changes in radar backscatter coefficient that are controlled by changes in soil moisture content following the selected precipitation event. Examination of the RGB color composite (Fig. 2a) shows two major shades of colors, red, and cyan. Areas that show higher moisture content following the rain event will experience an increase in backscatter coefficient and will thus appear in shades of red, while areas that show no change in moisture content will appear in shades of cyan. Not all the areas that appear in shades of cyan are areas showing no change in moisture content; some of them show no change in radar backscatter because they are not adequately visible to the radar sensor.

Terrain visibility to the radar satellite sensor depends on the orientation of the satellite line of sight (LOS) and radar acquisition geometry with respect to that of the surface. Visibility thereby varies within different portions of the same scene depending on local incidence angles, which, in turn, are determined by local terrain slope and aspect (Cigna et al. 2014). We estimated the "R-index" (Notti et al. 2010, 2011) to synthesize the effects of local topography (slope and aspect parameters) and satellite LOS parameters (incidence angle and azimuth). R-index values (range -1 to $+1$) exceeding 0.2 represent targets with medium-to-very good exposure to satellite LOS, negative values are indicative of layover and foreshortening and are unresolved, and those in between ($0 < R < 0.2$) have medium visibility. The R-index values were multiplied by 100 (Fig. 2b). Less than 10 % of our area was found to be unresolved; the remaining areas have medium-to-excellent radar visibility (Fig. 2a, b). Thus, the overall terrain visibility to radar imagery was deemed satisfactory.

Next, we demonstrate that the distribution of the red areas on Fig. 2a correlates with the distribution of wadis, faults, shear zones, and mafic dikes that were identified in the field, and using remotely acquired data sets, we show how these features and structures were delineated from remotely acquired data.

3.4 Identification of the Nature of the Water-Bearing Features from Digital Elevation Models and VNIR Images

Digital elevation models (DEMs) and two types of VNIR images were used to identify the nature of the moisture-bearing features: Landsat 7 TM images and Google Earth images. Landsat 7 acquires reflected light in eight spectral bands, four of which are in the VNIR wavelength region, two in the shortwave infrared, one in thermal infrared, and one panchromatic. A pair of Landsat 7 TM images were used to generate false-color composites over the entire Feiran watershed. Atmospherically corrected reflectance data were
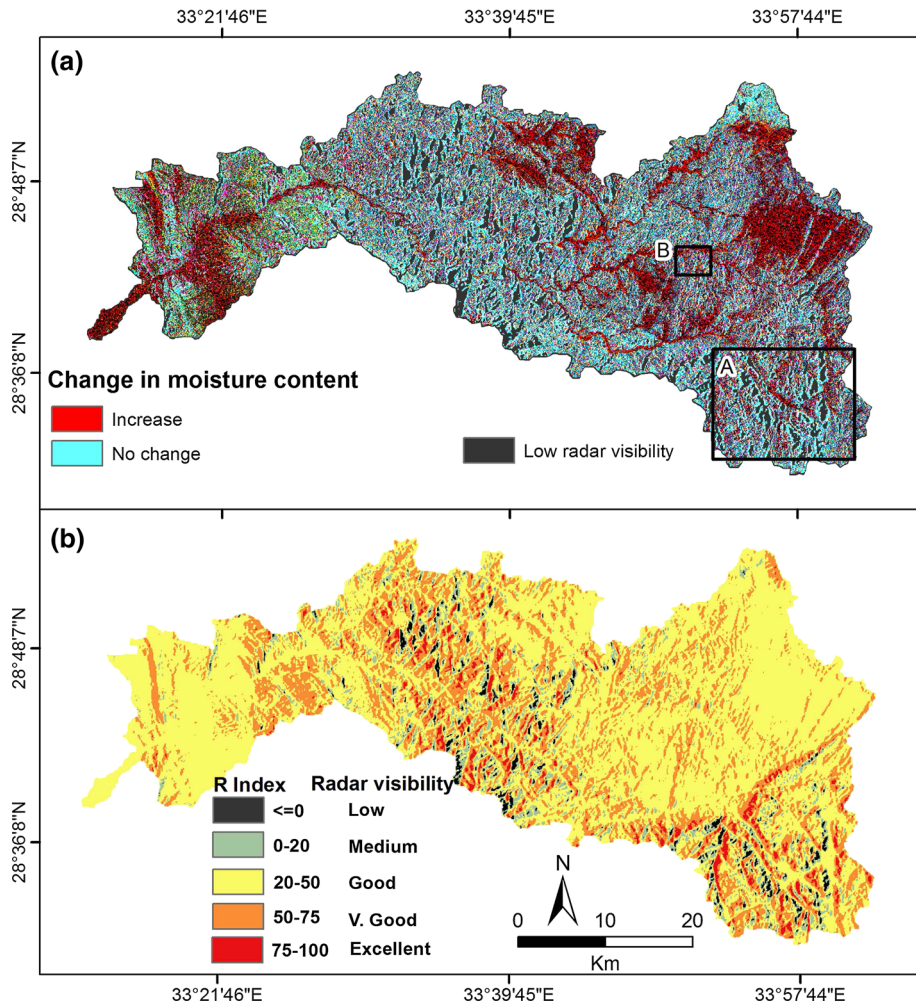
Fig. 2 a Envisat ASAR false-color composite normalized difference image for the Feiran watershed showing changes in radar backscatter coefficient following a precipitation event on 17–18 January 2010; the composite was generated from a radar image acquired before (11 and 27 November 2009) and after (20 January and 5 February 2010) the precipitation event. Areas that witnessed an increase in soil moisture following the precipitation appear in shades of *red*, those experiencing no or minor change in soil moisture appear in shades of *cyan*, and areas that are unresolvable on radar imagery are shown in shades of *gray*. Enlargement of *boxes A* and *B* on **a** are shown in Figs. 4 and 5, respectively. **b** R-index image shows the effects of local topography (slope and aspect parameters) and satellite LOS parameters (incidence angle and azimuth) on the resolving power of radar backscatter images

extracted from digital numbers following the procedures described in Sultan et al. (1987). False-color mosaics of VNIR TM band ratio color composite images were used to delineate major structural elements (width >30 m) [i.e., dikes (mafic and felsic), fault traces, and shear zones]. Other structural elements (width <30 m) were delineated using high-resolution Google Earth images.

3.4.1 Delineating Wadi Networks

Valleys generally appear as bright areas on Landsat TM bands, compared to the darker surrounding mountainous terrains (Fig. 3a). The stream network and watershed boundary for the Feiran watershed (Fig. 3b) were extracted from the DEM using the TOPAZ technique (Jensen and Domingue 1988; Martz and Garbrecht 2002) and were validated by comparisons to TM individual bands (Fig. 3a). Inspection of Fig. 2a shows that many of
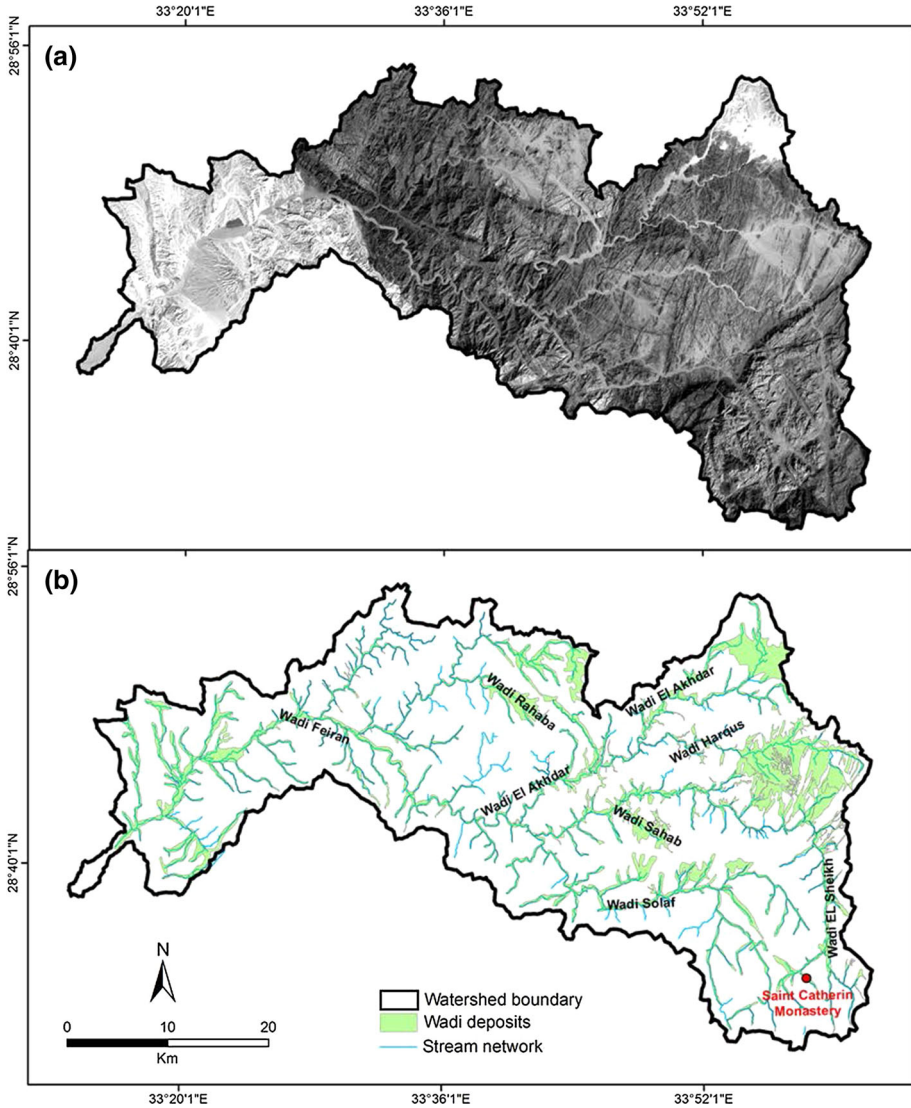
Fig. 3 Distribution of wadi networks in the Feiran watershed. **a** Landsat TM band 5 image showing bright wadis compared to the surrounding mountainous terrains (*dark terrain*). **b** DEM-derived wadi network and watershed boundary

the areas experiencing an increase in moisture on the radar imagery mosaic correspond to the distribution of: (1) the observed wadis network, represented by bright areas on TM band 5 image (Fig. 3a), and (2) the wadi network derived from DEM (Fig. 3b).

3.4.2 Delineating Faults and Shear Zones

The criteria used for the identification of faults and shear zones in the field and from satellite imagery (TM band ratio color composites and Google Earth images) include: (1) the presence of lithologic linear discontinuities that are tens of meters (faults) to hundreds of meters (shear zones) wide, (2) the presence of subparallel topographic ridges within the inferred shear zones, seen in individual band TM images that are probably caused by differential weathering of compositionally different lithologic units in the shear zones, (3) the lateral displacement and/or reorientation of outcrop patterns of distinctive lithologies and structural trends to align with inferred fault or shear zone in case of strike-slip displacements, and (4) the sense of lateral displacement on strike-slip faults that could be inferred from the changes in direction of structural trends and outcrop pattern of distinctive lithologies as they approach the inferred fault or shear zone. Because the examined satellite images are looking down on Earth, they are ideal for detecting lateral displacement along strike-slip faults and shear zones, but are less effective in mapping dip-slip displacement.

Inspection of Fig. 4a (enlargement of box A; Fig. 2a), the VNIR TM band ratio color composite (Fig. 4b), geologic maps (Klitzsch et al. 1987), and our field observations show that some of the areas showing an increase in moisture content on the radar image correspond to the distribution of: (1) previously mapped faults and shear zones (Klitzsch et al. 1987), many of which we verified in the field (Fig. 4c), and (2) numerous lithologic and structural trends of various scales.

Field observations and examination of Fig. 4a–c show that these sigmoidal features display the following characteristics: (1) many are subtended between adjacent and subparallel faults of similar orientation (largely northwest or northeast faults), (2) their sizes range from tens of meters to kilometers in length and from tens to hundreds of meters in width, (3) their sigmoidal shape arises from reorientation of the original lithologic layering or structural trends to align with the direction of the bounding faults or shear zones, (4) they are highly deformed areas probably because they incorporate intersecting multiple generations of fractures, faults, and shears, and (5) they generally have topographic expressions (e.g., ridge or valley) and/or lithologic expressions (compositional layering). We interpret these observations to indicate that these sigmoidal features represent planes of weakness (fractures, faults, and shear zones) that deformed by younger strike-slip fault systems, causing them to reorient and realign with the trends of the fault and shear systems.

3.4.3 Delineating Mafic and Felsic Dikes

The criteria used for the identification of mafic and felsic dikes in the field and from satellite imagery are: (1) subparallel, compositionally homogenous, linear features of large areal extent (hundreds of meters) and limited width (meters) that cut across rock units and sediments of variable compositions, (2) mafic dikes rich in Fe-bearing aluminosilicates (pyroxene) and opaque phases (magnetite, ilmenite) and poor in hydroxyl-bearing phases (Iacumin et al. 1998; El-Sayed 2003) appear in shades of blue on the band ratio color composite and as dark streaks on the Google Earth images, while felsic dikes, which are
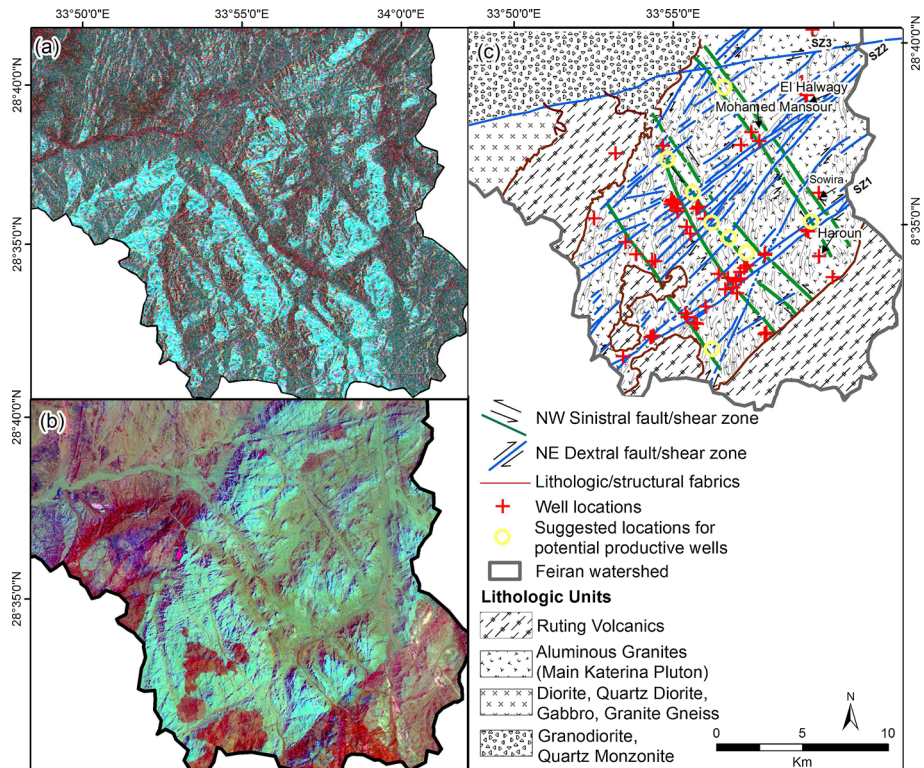
Fig. 4 Satellite imagery and interpretation map for area covered by *box A* in Fig. 2a. **a** Envisat ASAR false-color composite normalized difference image of the Saint Catherine area. **b** TM band ratio color composite (5/4 × 3/4: *blue*; 5/1: *green*; 5/7: *red*) color composite image. **c** Interpretation sketch map showing the distribution of faults and shear zones that was extracted from **a**, **b** and published geologic maps (Klitzsch et al. 1987), observed well locations that were extracted from field observations and Google Earth images (*red cross*), and potential productive well locations at the intersections of shear zones (*open yellow circle*)

poor in Fe-bearing aluminosilicates, opaque phases, and hydroxyl-bearing phases (Iacumin et al. 1998; El-Sayed 2003) appear in shades of green (fresh), and brown (slightly altered) on the ratio images (Sultan et al. 1987) and as bright buff linear features areas on the Google Earth images.

Inspection of Fig. 5a (enlargement of box B; Fig. 2a), the Google Earth image (Fig. 5b), the band ratio color composite (Fig. 5c), geologic maps (Klitzsch et al. 1987), and our field observations shows that some of the linear features showing an increase in moisture content on the radar imagery mosaic (e.g., a–a′, b–b′, c–c′; Fig. 5) correspond to the distribution of previously mapped mafic dikes, many of which we verified in the field, on Google Earth images (Fig. 5b), and on band ratio color composite (linear blue features; Fig. 5c). None of the investigated felsic dikes show an increase in moisture content on the radar imagery mosaic. The mafic dikes, but not the felsic, are fractured and weathered, especially at their contact with the country rock. We suspect that the weathered and fractured margins of mafic dikes and their surrounding country rock could provide preferential zones for infiltration and groundwater flow.
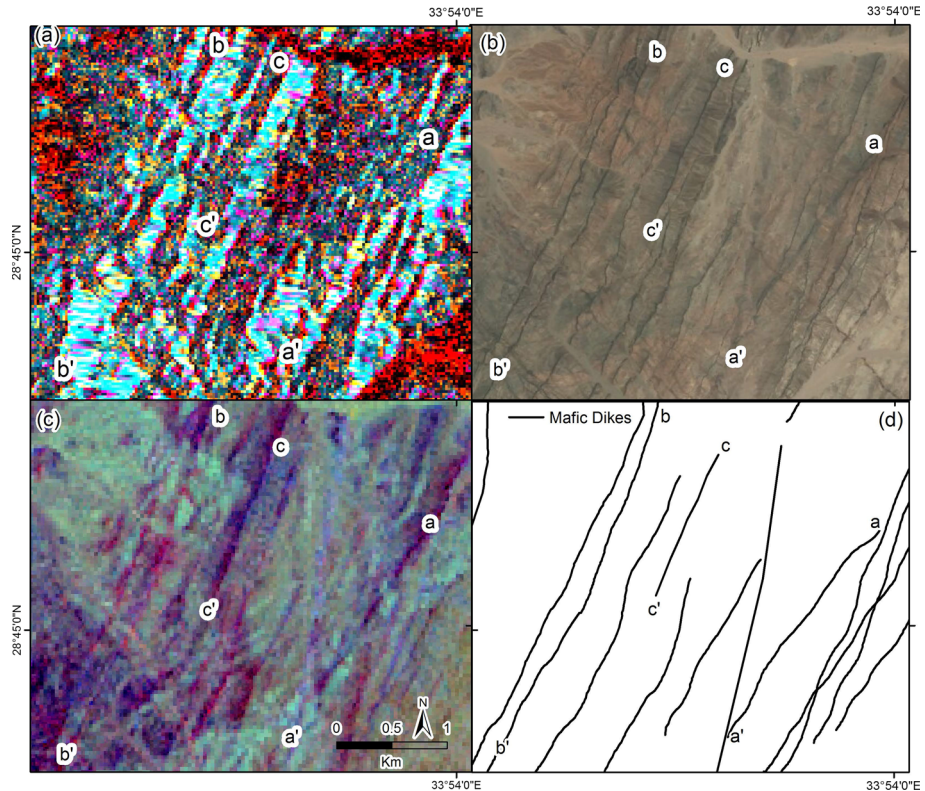
Fig. 5 Satellite imagery and interpretation map for area covered by *box B* in Fig. 2a. **a** Enlargement of Envisat ASAR false-color composite normalized difference image, showing the *red shades* surrounding the weathered mafic dike margins. **b** High-resolution Google Earth image shows mafic dikes in *greenish* to *dark green lines*. **c** TM band ratio color composite (5/4 x 3/4: *blue*; 5/1: *green*; 5/7: *red*) image representing mafic dikes in *blue shades* according to their composition (plagioclase, pyroxene, and amphibole). **d** Interpretation sketch map extracted from **a**–**c** and published geologic maps (Klitzsch et al. 1987)

3.5 Testing (Field Geophysics) Whether the Satellite-Based Water-Bearing Features are Preferred Pathways for Groundwater Flow

Field observations and magnetic data were used to define the postulated extension of the satellite-based water-bearing features in the wadis. VLF techniques were then used to examine the presence or the absence of conductive subvertical layers in these locations.

3.5.1 Delineating the Postulated Extension of Dikes, Shear Zones, and Faults in Wadis

Magnetic methods were used to define the postulated extension of the dikes that were identified using satellite (VNIR) data under the alluvial fill flooring the wadis, and to investigate the subsurface geometry of the dikes in selected locations. The magnetic method is a time- and cost-effective method that measures anomalies in the Earth's magnetic field to investigate the nature of subsurface geology. The Earth's rocks' magnetic

content is variable and depends on the type of rock and the environment in which the rock resides. Common causes of magnetic anomalies include, but are not limited to, the juxtaposition of rock units of varying magnetic susceptibilities. This usually occurs where faults and/or dikes are surveyed; they show as peaks or troughs as the profile crosses the investigated dike or fault plane (Telford et al. 1990).

The Canadian Scintrex MFD-4 fluxgate magnetometer was used to measure the vertical component of total magnetic field (measured in nanoteslas) along transects within the Feiran watershed. Figure 1c shows the locations of the magnetic profiles. The vertical component of the magnetic field, location (latitude and longitude), and time of acquisition were recorded for every measured field station. Because the Earth's magnetic field is subject to diurnal variations, each surveying day was started and ended with base station readings that were used to correct for drift corrections. Magnetic data were collected (seven profiles, with a station interval of 1–5 m, in September 2011) in Wadi El Shiekh (Fig. 1c) and surroundings. Figure 6a, b shows magnetic profiles (m03, m04) that were conducted across selected mafic dikes in Wadi El Sheikh showing high magnetic susceptibilities (peaks ranging from 28,902 to 29,390 nT) compared to their surroundings, probably due to their higher magnetic content. Magnetic profiles were also used to delineate the postulated extension of faults and shear zones in the wadis. Figure 6c shows magnetic reversals along a south–north-trending profile (m01) as two subparallel strands of a northeast-trending shear zone were crossed in Wadi El Sheikh. This response is probably due to shear zone-related lateral displacement that juxtaposed rock units of varying magnetic susceptibilities.

A three-layer two-dimensional (2D) modeling was carried out after removing the linear regional field from each of the selected profiles. The model parameters (total magnetic
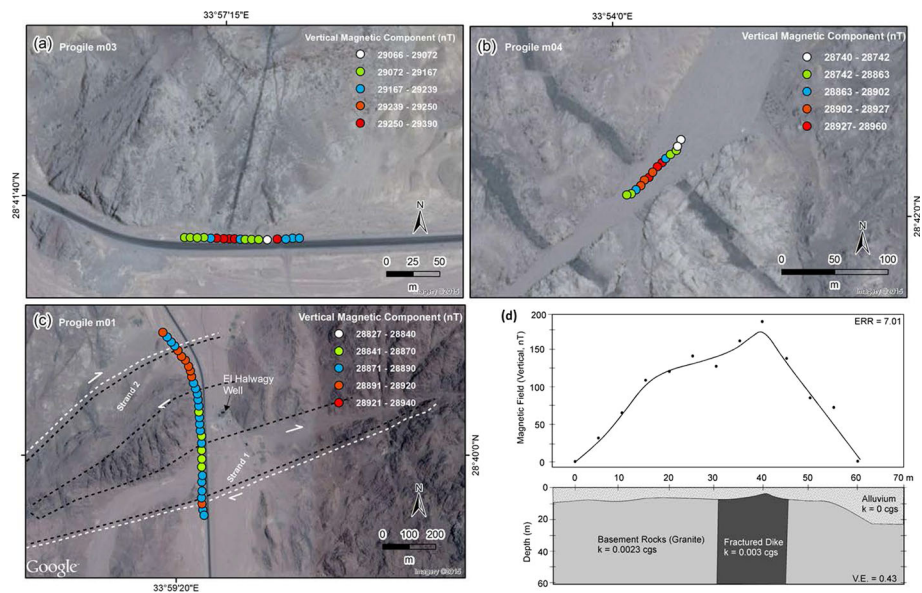
Fig. 6 Selected magnetic profiles verifying the extension of mafic dikes under the alluvial fill in wadis. **a** West–east-trending magnetic profile (m03) intersecting north–south-trending dike (thickness 7 m). **b** Southwest–northeast-trending magnetic profile (m04) intersecting northwest–southeast-trending dike. **c** South–north-trending magnetic profile (m01) in Wadi El Sheikh, intersecting strands of an east-northeast-trending shear zone. **d** 2D magnetic model along profile (m04)

field: 42,187 nT; inclination: 40.9°; declination: 2.4°) were extracted from the National Oceanic and Atmospheric Administration (NOAA: http://www.ngdc.noaa.gov/geomag/magfield.shtml). Figure 6d shows the 2D inversion results for the SW–NE-trending profile (m04). In this model, the surface layer [the alluvium sediments; magnetic susceptibility $(k) = 0$ cgs] overlies a layer of granitic basement rock ($k = 2.3 \times 10^{-3}$ cgs), which in turn is dissected by a mafic dike ($k = 3.0 \times 10^{-3}$ cgs). In the SW and central parts of the profile, the thickness of the alluvium layer is uniform (range 8–10 m); in the NE, the alluvium layer thickness increases reaching ~ 20 m. The mafic fractured dike was centered in the middle of the profile with an average width of ~ 14 m. The extracted geometric parameters could be useful in prospecting for groundwater if the targeted feature (dyke, fault, shear zone) was water-bearing.

3.5.2 Detecting Conductive Subvertical Layers Along Water-Bearing Features (Shear Zones, Faults, and Mafic Dikes) and Their Postulated Extension in Wadis

The VLF electromagnetic method was used to verify the presence of groundwater along the identified structures (shear zone, fault, and mafic dike) within the Feiran watershed. The VLF method is an ideal geophysical technique in our case because of its effectiveness in detecting conductive water-saturated subvertical breccia zones in bedrock (Palacky et al. 1981). The VLF method uses the radio carrier waves of the submarine communications stations of the various navies of the world. The radiated electromagnetic field from a remote VLF transmitter consists of a vertical electric field component and a horizontal magnetic field component, each perpendicular to the direction of propagation. The VLF receiver measures the distortion of the normally horizontal electromagnetic VLF flux lines by local electrical conductors. For each field stop, the receiver records the frequency of the transmitting station, the tilt of the magnetic field, ellipticity in the vertical and horizontal planes, and signal strength (Klein and Lajoie 1980; Paterson and Ronka 1971).

The VLF technique has some limitations including, but not limited to: (1) the VLF receiver responds strongly to massive sulfides, as well as to graphitic shear zones. However, the Feiran watershed is not known to contain these types of sulfide deposits and shear zones, so it is unlikely that interference would present itself in this form. (2) The VLF receiver is limited to detection within an approximately 90° fan of strikes (±45° from the radial azimuth to the transmitting station). To adjust for this, the VLF measurements were taken using two transmitting stations. (3) VLF measurements are subject to sudden pulsations from the solar wind, which result in rapid deviations of the apparent measured tilt angle that can last for several minutes. In the event that such disturbances were encountered, data collection was paused or repeated to rule out this possible interference source.

In this study, VLF profiles were collected using an IRIS T-VLF receiver along transects in Wadi El Sheikh and wadis surrounding the Saint Catherine area. Throughout three (September 2011, June 2012, and July 2013) field trips, 11 sites were visited and a total of 43 VLF profiles were collected (Fig. 1c). In the selection of profiles, we collected VLF data along transects that are as close as possible to being orthogonal to the strike of radar-based investigated structural features (faults, dikes, shear zones). Transects ranged in length from 220 to 940 m, with a station separation of 10 and 20 m. Two main transmitting stations were selected because of their strong signals (England: GBZ, 19.6 kHz; and Germany: NPM, 23.4 kHz); these stations provided ideal geometries for targeting north–south- and northwest–southeast-trending structural elements along east–west- or northeast–southwest-trending profiles.

VLF data could be examined on tilt angle versus profile distance plots; on these plots, conductors (i.e., water-saturated subvertical breccia zones) are located where the tilt angle changes sign (zero crossover). Alternatively, simple filtering can be applied to remove short-wavelength features (e.g., single-station anomalies) and to shift the peaks by 90°. We applied a four-point Fraser filter (Fraser 1969) to all of the collected 43 VLF profiles; on these plots, the positive peaks are directly over the conductors.

A northeast–southwest-trending VLF profile (1305; Fig. 7) was conducted along a transect perpendicular to a northwest-trending sinistral shear zone that defines the location of a wadi (average width: 200 m) which intersects Wadi El Sheikh. The northwest-trending shear zone (defined by black dashed lines; Fig. 7a–c) is characterized by subparallel topographic ridges and interleaving wadis. As the shear zone is approached, all structural elements (e.g., ridges or valleys) reorient to align with the shear zone (e.g., yellow lines, Fig. 7b). These structural trends appear as blue and dark green streaks (ridges) separated by subparallel pale green streaks (valleys) on the band ratio color composite (Fig. 7a), as subparallel northwest-trending red streaks (wadis) separated by cyan areas (ridges) on
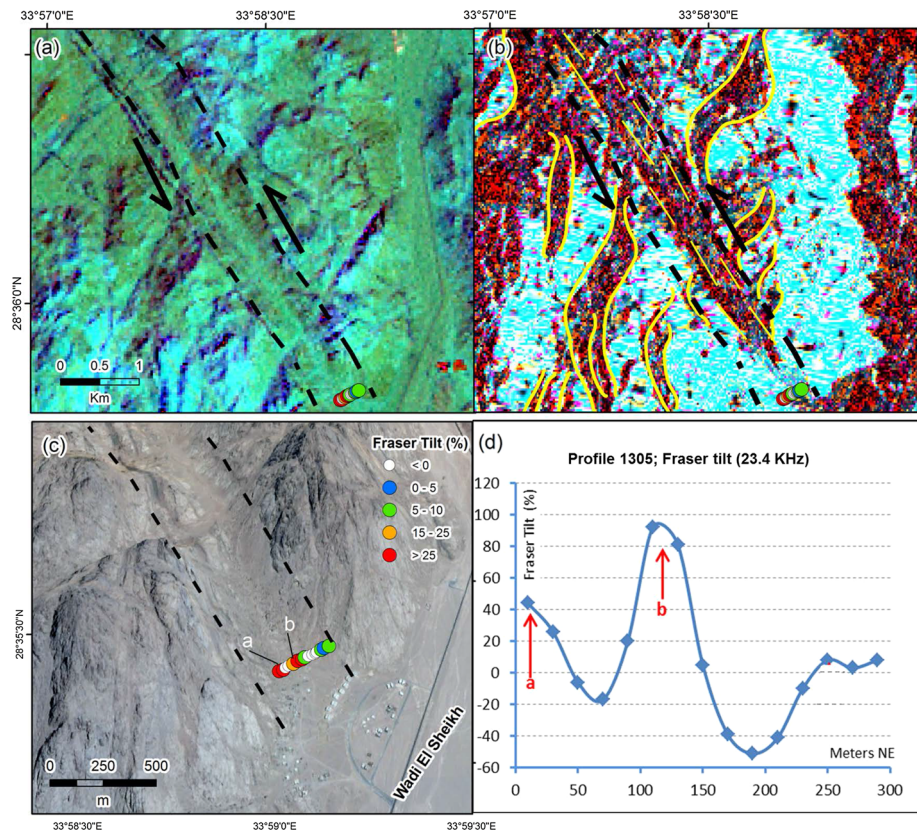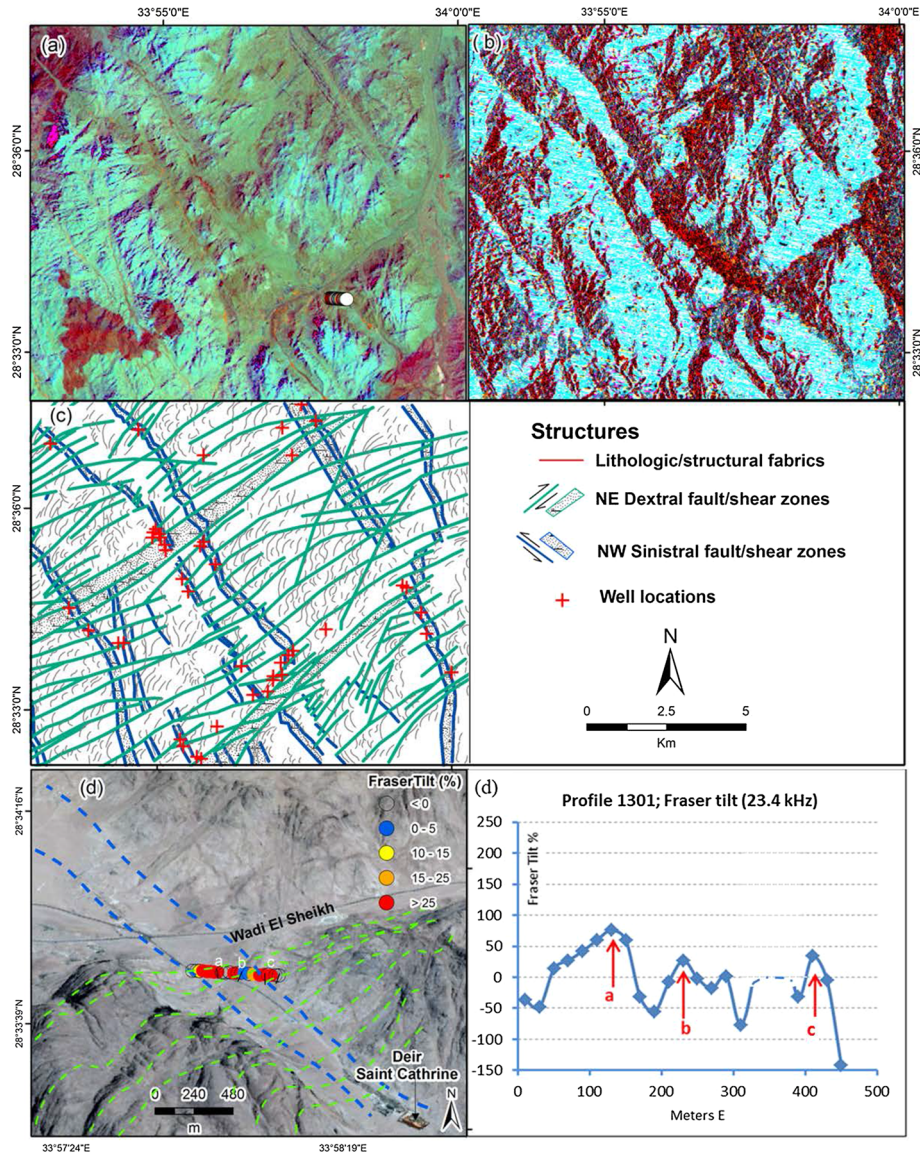

Fig. 7 Use of VLF data (VLF profile 1305; Fig. 1) to verify the conductive nature of the sinistral northwest–southeast-trending shear zone. **a** Band ratio color composite image. **b** Envisat ASAR false-color composite normalized difference image. **c** Google Earth image showing the location of the southwest–northeast-trending VLF profile with respect to the shear zone. **d** VLF profile 1305. Also shown are the boundaries (*dashed black line*; **a–c**) of the northwest–southeast-trending shear zone and lithologic and structural trends (*yellow lines*; **b**)

Envisat ASAR false-color composite normalized difference image (Fig. 7b), and as sub-parallel ridges (bright ridges) separated by sparsely vegetated valleys (darker valleys) on the Google Earth image (Fig. 7c). At the onset of the profile, a large anomaly (Fraser tilt location "a" > 40 %; Fig. 7d) was observed, and halfway through the profile, an even larger anomaly (Fraser tilt location "b" 90 %; Fig. 7d) was recorded at the intersection of the profile with narrow (<10 m in width) wadis within the shear zone. Additional VLF profiles (1107, 1102, 1206, and 1313) were measured across additional northwest-trending shear zones, all of which showed one or more peaks with Fraser tilt ranging from 15 to 20 %, indicating that many of these northwest-trending shear systems act as conductive subvertical layers.

The Saint Catherine area is dissected by another major set of shear zones trending northeast to east-northeast with dextral motion (Fig. 4d). A south–north VLF profile (profile 1103) was conducted along Wadi El Sheikh perpendicular to a major east-north-east-trending shear zone (defined by black dashed lines; Fig. 8a, b). A close up (Fig. 8c) reveals that the dextral displacement along the shear zone is concentrated along strands within the shear zone where intense brittle deformation was observed in the field. A southern strand extends along an east-northeast tributary of Wadi El Sheikh and a northern
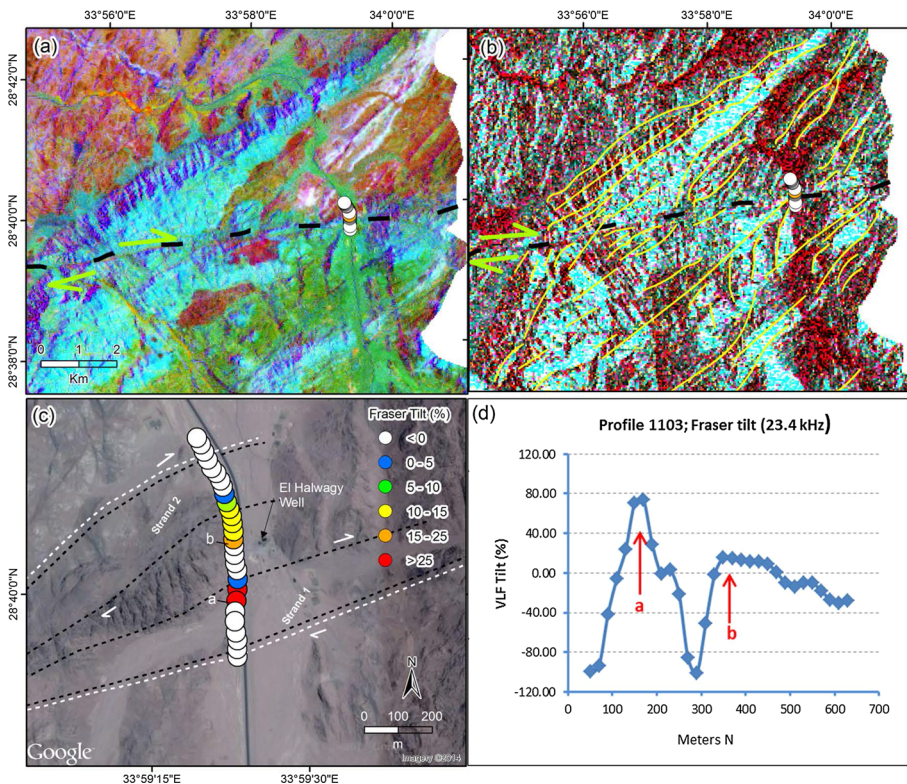
Fig. 8 Use of VLF data (VLF profile 1103; Fig. 1) to verify the conductive nature of the dextral east-northeast-trending shear zone. **a** Band ratio color composite image. **b** Envisat ASAR false-color composite normalized difference image. **c** Google Earth image showing the location of the south–north VLF profile (1103) with respect to the ENE-trending strands of intense brittle deformation (*black dashed lines*) within the shear zone (*white dashed lines*). **d** VLF profile 1103. Also shown are the boundaries of the east-northeast-trending shear zone

strand passes by a productive well (El Halwagy well) in Wadi El Sheikh. These strands are characterized and bordered by subparallel topographic ridges (blue streaks, Fig. 8a; cyan streaks; Fig. 8b; dark ridges, Fig. 8c) and valleys (pale green, Fig. 8a; red streaks: Fig. 8b; bright valleys, Fig. 8c). The Fraser-filtered data showed a peak (Fraser tilt location "a" > 70 %; Fig. 8d) at the intersection of the postulated extension of the southern strand and Wadi El Sheikh and another (Fraser tilt location "b" 20 %; Fig. 8d) further north along the intersection of the northern strand with Wadi El Sheikh. Additional VLF profiles (1303, 1307, 1308, 1309, and 1310) were measured across numerous east-northeast-trending shears. For all except profile 1308, large tilt angles (17–25 %) were measured, indicating that many of the shear systems act as conductive subvertical layers, and by inference contain water.

A west–east-trending profile (1301; Fig. 9a–e) was conducted along the wadi that leads to the Dier (Monastery) Saint Catherine (Fig. 9d); the wadi is defined by a major north-west–southeast-trending sinistral shear zone (blue dashed lines, Fig. 9c, d). The sinistral shear system is intersected by a dextral northeast–southwest-trending shear system (green dashed lines, Fig. 9c). These northwest- and northeast-trending shear zones appear in shades of red on the radar mosaic (Fig. 9b). As the shear zones are approached, all earlier structural elements and fabrics are reoriented to align with the trend of the shear zone (e.g., gray lines; Fig. 9c, d). Along the shear zones, subparallel topographic ridges and valleys are observed in the band ratio color composite and/or wide valley as is the case with the northwest shear zone (Fig. 9a). VLF profile 1301 intersects the northwest–southeast- and the northeast–southwest-trending shear zones, both of which appear in shades of red in the Envisat ASAR false-color composite difference image, indicating increased soil moisture following the 17–18 January 2010 rain event (Fig. 9b). The Fraser-filtered data (Fig. 9e) showed high tilt angles (location "a" 76 %, "b" 27 %, and "d" 34 % at the intersection of the postulated extension of the northwest shear zone and northeast-trending faults marking the locations of valleys separating subparallel topographic ridges) (Fig. 9a). Examination of Fig. 9b shows that many of the moisture-bearing areas appear as sigmoidal features subtended by pairs of sinistral northwest- or dextral northeast-trending faults or shear zones. The sigmoidal shape results from the realignment of structural trends and fabrics to align with the direction of the subtending faults and shear zones.

A northeast-trending profile (1106: Fig. 10a, c) was measured in El Berkah area across a northwest-trending mafic dike (13 m in thickness); the dike is dissected by north-northeast-trending shear zones, (Fig. 10a). The word "Berkah" in Arabic means a "pool of water"; the name was assigned by the bedouins to refer to a pool of water where the dike intersects the wadi, also the location of a small farm that collects water channeled by the mafic dike (Fig. 10b). Figure 10c is an enlargement of the box in Fig. 10a which shows the highly weathered and fractured zone that surrounded the mafic dike margins. Tilt angles were high (11–20 %; Fig. 10d) at the weathered country rocks around margins of the mafic dike, compared to the central part of the dike (Fig. 10d). The dike margins were chilled, weathered, and fractured, as were the intruded country rocks, whereas the central parts of the dike were massive and fresh. Additional VLF profiles (1101, 1104, 1105, 1106, 1108, 1109, 1110, 1201, 1202, 1203, 1204, 1209, and 1215) were measured across numerous mafic dikes. For all measured profiles, measured tilt angles ranged from 20 to 25 %, indicating that the mafic dikes' margins and the fractured and intruded weathered zone surrounding the dike act as conductive subvertical layers, with the exception of VLF profiles 1110, 1203, and 1204 because their margins were not weathered or fractured.

Fig. 9 Use of VLF data (VLF profile 1301; Fig. 1) to verify the conductive nature of the sinistral northwest–southeast shear zone and the sigmoidal features. **a** Band ratio color composite image. **b** Envisat ASAR false-color composite normalized difference image. **c** Interpretation map based on **a**, **b** showing northwest–southeast sinistral shear zones/faults (*blue lines*) dissected by northeast–southwest-trending faults/shears (*green lines*), lithologic and structural trends (*gray lines*), and well locations (*red crosses*). **d** Google Earth image showing anomalies (*red* and *orange circles*) along a west–east VLF profile (1301) at the intersection of a northwest–southeast shear zone (*blue dashed lines*) and the postulated extension of highly deformed sigmoidal features (*green dashed lines*). **d** VLF profile 1301
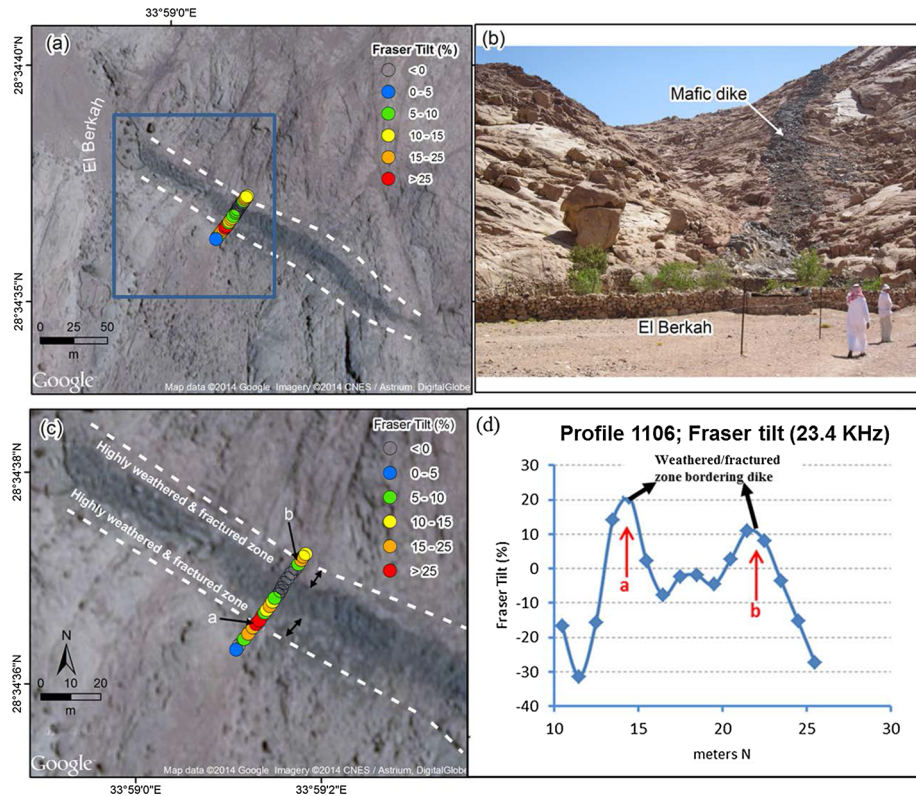
Fig. 10 Use of VLF data (VLF profile 1106; Fig. 1) to verify the conductive nature of the weathered and fractured margins of mafic dikes and their surrounding country rock. **a** Google Earth image showing a northwest–southeast-trending mafic dike, intruded country rock, and surrounding highly weathered and fractured zones observed in the field. **b** Field photo (facing the southeast direction) showing a green area at the intersection of a mafic dike with a wadi (El Berkah area). **c** Enlargement of the area outlined by the *blue box* in **a** showing anomalies (*red* and *orange circles*) along a southwest–northeast VLF profile (1106) at the intersection of the profile with the weathered and fractured dike margins and surrounding country rocks. **d** VLF profile 1106

3.6 Investigating the Impact of Conductive Features on Groundwater Flow

An approximate potentiometric surface map (Fig. 11a) was prepared from water levels of 52 wells (Aggour 2007) tapping the fractured basement and the alluvium aquifers in the Feiran watershed. The map is intended to provide the approximate potentiometric surface wherever the more permeable domains (e.g., alluvial aquifers and fractured basement) occur but not in the intervening massive basement. An elevation profile (86 km long) was generated along the entire length of the Feiran watershed in Wadis El Sheikh and Feiran (Fig. 11a) and compared to groundwater levels in 18 wells flooring the two wadis (Fig. 11b). Examination of Fig. 11a reveals a general correspondence between topographic and groundwater gradients in the Feiran watershed, consistent with previously published work that indicates that the groundwater flow in mountainous regions is controlled by topography on the regional scale (Toth 2009; Gaber et al. 2009). However, Fig. 11 also
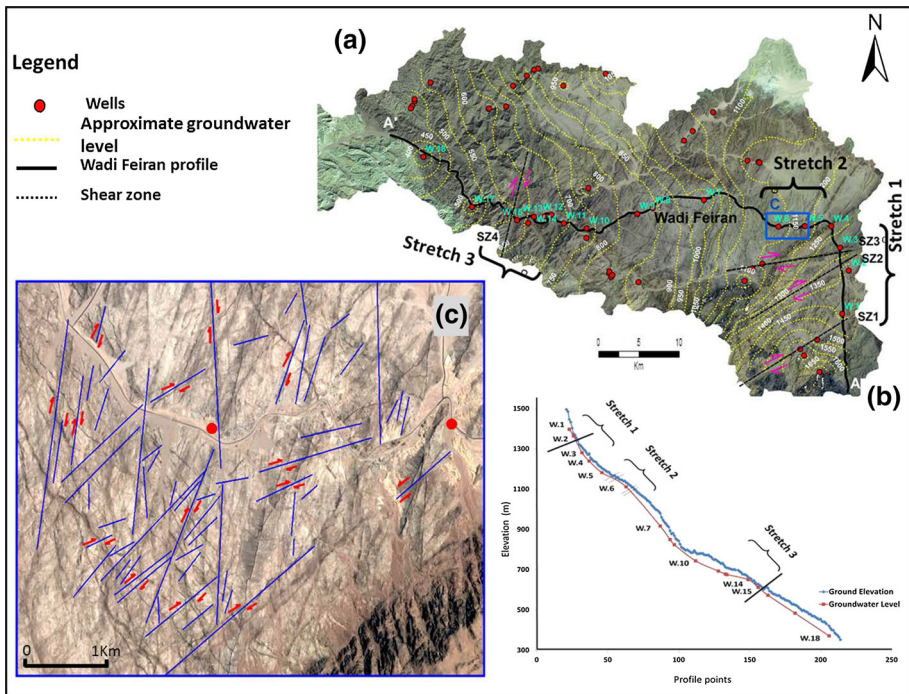
Fig. 11 **a** Landsat TM image over the Feiran watershed showing the approximate groundwater levels (*dashed yellow contours*), and the regional groundwater flow direction; also shown are locations of traverse A–A′ along Wadi El Sheikh and Wadi Feiran, sections (*stretches 1, 2, and 3*) along traverse A–A′ where shallow groundwater levels were reported, well locations along traverse A–A′, and the distribution of shear zones (SZ1, SZ2, SZ3, and SZ4). **b** Profile along traverse A–A′ showing ground surface elevation, groundwater elevation, and sections (*stretches 1, 2, and 3*) along the traverse where shallow groundwater levels were reported. **c** Enlargement of area covered by *blue box* in **a** (*stretch 2*) showing the distribution of dike swarms (*dark streaks*) that are intensively displaced by dextral faults (outlined by *blue lines*), most of which are dextral in nature

reveals a spatial correlation between the distribution of major structural elements and shallow groundwater levels upstream from the major shear zones in the Feiran watershed.

4 Discussion and Regional Implications

Because the basement complex in the Feiran watershed is largely massive, the groundwater flow is expected to occur along the more permeable domains represented by the alluvial aquifers flooring the wadi network and by the fractured basement within shear zones, faults, fractures, and mafic dikes. The structural control of groundwater flow locally has been documented in earlier studies (Issar and Gilad 1982; Kusky et al. 1998).

We interpret the observed spatial correspondence of the satellite-based water-bearing features following precipitation events with the location of wadis, major northwest–southeast- or northeast–southwest-trending shear zones and faults, fractures, and mafic dikes as indicating preferred pathways for surface or near-surface water flow along these topographic or structural features. The presence of VLF anomalies along almost all (85 %)

of the investigated features indicates that these features, hereafter referred to as "conductive features," are in general preferred pathways for groundwater flow as well. Because the conductive features have higher porosity and permeability compared to their massive surroundings, infiltration through transmission losses will occur along their length. The depth to where infiltration will occur will depend on the thickness of the permeable zone, namely the thickness of the alluvial aquifer in wadis and the vertical thickness of the permeable zone in faults and shear zones, or within the weathered and fractured margins of mafic dikes and the country rock they intrude. A limited vertical thickness could explain why a few of the investigated features showed an increase in moisture content on radar imagery yet no VLF anomalies. If we were to generalize our findings, we can interpret the majority of the areas showing an increase in soil moisture following precipitation events (red areas on Fig. 2a) as the preferred pathways for groundwater flow. Thus, the groundwater flow is largely controlled by a complex network of preferred pathways encompassing wadis, shear zones, faults, fractures, and mafic dikes. It is reasonable to assume that the groundwater moves along these preferred pathways in ways that ultimately achieve the overall regional groundwater flow shown in Fig. 11a.

Conductive features that are subparallel to the groundwater flow direction are expected to capture groundwater flow (Gudmundsson 2000; Babikera and Gudmundsson 2004), whereas others that intersect the flow at high angles impound the groundwater upstream and reorient the groundwater flow to align locally with their respective trends (Gudmundsson 2000; Babikera and Gudmundsson 2004). The northwest- to north–south-trending features (Fig. 4d) that are subparallel to the regional groundwater flow direction will capture and facilitate the flow along its length, whereas the northeast-trending features that intersect the groundwater flow at high angle (>45°) will obstruct the flow and impound it in the upstream direction. Groundwater levels extracted from 18 wells in Wadi El Sheikh show evidence for impoundment of groundwater in three major stretches along the traverse ("stretch 1," "stretch 2," and "stretch 3"; Fig. 11). Stretch 1 encompasses the area upstream of one or more of three major northeast-trending shear zones (SZ1, SZ2, SZ3: Figs. 4b, 11a, b). Stretch 2 is located within and upstream of an outcrop of G2 granite that is intensively dissected by northeast-trending right-lateral strike-slip faults (Fig. 11c), as evidenced by the observed displacements of the dike swarms at their intersections with the faults. Stretch 3 is upstream from a major northeast-trending shear zone (SZ4, Fig. 11a, b). If the northeast-trending shear zones and dike swarms are impeding groundwater flow, one would expect to observe (1) elevated groundwater levels within and upstream from the areas dissected by the shear zones and dikes, and (2) a drop in groundwater level downstream from these areas. Inspection of Fig. 11 shows that this is indeed the case. Stretch 1 within and upstream from shear zones SZ1, SZ2, and SZ3, stretch 2 within and upstream from the highly faulted dike swarm area, and stretch 3 upstream from shear zone SZ4 display a relatively shallower groundwater depth compared to neighboring areas lacking these features.

The intersections of the northwest- and northeast-trending shear zones enhance porosity and create conditions favorable for hosting groundwater in fractured basement rocks. This conceptual model is supported by: (1) the presence of productive wells at the northwest- and northeast-trending shear zones in the Feiran watershed (Haroun, Zeitona, El-Watia, and Sahab wells; red crosses, Figs. 1, 4c) and (2) conventional resistivity data (Shendi and Abouelmagd 2004) at these four locations that revealed thick, saturated, fractured, basement aquifer at these intersections (Haroun well: 13.8 m; Zeitona well: 10 m; El-Watia well: 8.7 m; Sahab well: 14.3 m) compared to thin (few meters) fractured basement aquifer upstream and downstream from the intersection locations. Our findings suggest additional

potential groundwater accumulations are likely to be found at the intersection of the northeast- and northwest-trending shear zones in the Saint Catherine area. These locations for potential productive wells are represented by open yellow circles on Fig. 4c.

Similar findings were observed in central Sinai in areas north of the Feiran watershed. Examination of the head data from 25 deep wells (Rosenthal et al. 2007) tapping the Lower Cretaceous aquifer NSAS (Fig. 1) reveals structural control on groundwater flow. The south–north groundwater flow (Abouelmagd et al. 2014) in the NSAS is intercepted by orthogonal (east–west-trending) dextral shear zones, the most prominent of which is the Themed shear zone (TS) and the Sinai Hinge Belt (SHB) (Moustafa et al. 2013) (Fig. 1). As is the case with the fractured basement aquifer, these shear zones impede the groundwater flow causing a considerable hydraulic head drop (e.g., across the TS, from 467 m to 248 m) and a dramatic change in the regional flow direction from a south–north trend toward the Mediterranean Sea to a southwest–northeast trend across political boundaries into Israel (Fig. 1).

5 Summary and Conclusion

We conducted an integrated approach using geophysical, remote sensing, and field data sets and applied GIS technologies (1) to investigate the role of structural elements in controlling groundwater accumulation and flow, and (2) to identify the distribution of aquifers in the fractured basement in the Saint Catherine area, southern Sinai, Egypt. The following steps were undertaken to achieve these goals. We identified the spatial and temporal precipitation events over the basement complex from TRMM data and extracted from it temporal change in backscattering values in radar following one of the identified precipitation events. The increase in backscattering was attributed to an increase in moisture content, and the areas showing the increase in backscattering values were identified as preferred pathways for surface water infiltration. To investigate the nature of these areas and/or features, we correlated their distribution with observations extracted from field observations, remote sensing, and published geologic data, and concluded that the moisture-bearing features are mostly fractures, faults, shear zones, mafic dike swarms, and wadi networks.

The majority of the investigated features were determined to be preferred subvertical pathways for groundwater flow as evidenced by the observed high Fraser-filtered VLF tilt values that were measured across the identified features. These features trend in various directions, and thus, locally, the groundwater flow is controlled by the conductive features; however, groundwater flow is controlled regionally by topography, as evidenced by the observed general correspondence between topographic and groundwater gradients. The general groundwater flow direction in the upstream is from the southeast to northwest, and thus, the northwest–southeast- to north–south-trending conductive features are more likely to capture the groundwater flow given that they intersect the flow at low angles; the northeast–southwest to east–west conductive features intersect the flow at high angles and impound the groundwater upstream. Because the northwest–southeast features capture the flow, whereas the northeast–southwest impede it, their intersections often represent areas of groundwater accumulation, as evidenced by the presence of productive wells at a few intersections. Similar findings were observed in central Sinai, where examination of the head data from 25 deep wells tapping the NSAS revealed structural control on groundwater flow. The south–north groundwater flow is impeded by the east–west-trending dextral TS

and SHB shear zones, as evidenced by considerable hydraulic head drop across the shear zones. The faults also cause a dramatic change in the regional flow direction from a south–north trend toward the Mediterranean to a southwest–northeast trend across political boundaries into Israel.

Deciphering groundwater flow in sedimentary aquifer systems is straightforward once head data become available; this is not the case in fractured basement aquifer systems. These systems are heterogeneous in their porosities and permeabilities, making groundwater flow only possible along preferred pathways that are largely controlled by the distribution and connectivity of wadi networks and structures. Our studies indicate that false-color composite normalized difference images (e.g., Figs. 2, 4a, 5a, 7b, 8b, 9b) could be used as a first-order map guide for the groundwater flow distribution in basement terrains. These findings should be further validated using geophysical methods similar to those applied in this study and others (e.g., seismic refraction, resistivity sounding and profiling, and ground-penetrating radar) that could provide a detailed 2D subsurface image. The advocated integrated (remote sensing, geophysics, field, and GIS) methodologies are straightforward, practical, and cost-effective, and could potentially identify the distribution of water resources in many similar arid fractured basement terrains worldwide.

References

Abouelmagd A, Sultan M, Sturchio N, Soliman F, Rashed M, Ahmed M, Kehew A, Milewski A, Chouinard K (2014) Paleoclimate record in the Nubian Sandstone Aquifer, Sinai Peninsula, Egypt. Quatern Res 81(1):158–167. doi:10.1016/j.yqres.2013.10.017

Agar RA (1987) The Najd fault system revisited; a two-way strike-slip orogen in the Saudi Arabian Shield. J Struct Geol 9(1):41–48. doi:10.1016/0191-8141(87)90042-3

Aggour TA (2007) Water resources of Wadi Feiran with emphasis on geomorphology and geology. Ann Geol Surv Egypt 29:357–387

Ahmed M, Sauck W, Sultan M, Yan E, Soliman F, Rashed M (2013) Geophysical constraints on the hydrogeologic and structural settings of the Gulf of Suez rift-related basins: case study from the El Qaa Plain, Sinai, Egypt. Surv Geophys 35:415–430. doi:10.1007/s10712-013-9259-6

Amer R, Sultan M, Ripperdan R, Ghulam A, Kusky T (2013) An integrated approach for groundwater potential zoning in shallow fracture zone aquifers. Int J Remote Sens 34(19):6539–6561. doi:10.1080/01431161.2013.804221

Babikera M, Gudmundsson A (2004) The effects of dykes and faults on groundwater flow in an arid land: the Red Sea Hills, Sudan. J Hydrol 297:256–273. doi:10.1016/j.jhydrol.2004.04.018

Bartov Y, Steinitz G, Eyal M, Eyal Y (1979) The development of the Arava Rift Valley and the Red Sea. New evidence for Cenozoic strike-slip faults in Eastern Sinai. Abstracts, annual meeting of Sede Boqer, Israel Geological Society, p 8

Blenkinsop TG, Kadzviti S (2006) Fluid flow in shear zones: insights from the geometry and evolution of ore bodies at Renco Gold Mine, Zimbabwe. Geofluids 6:334–345. doi:10.1111/j.1468-8123.2006.00154.x

Bosworth W, McClay K (2001) Structural and stratigraphic evolution of the Gulf of Suez rift, Egypt: a synthesis. Mém Mus Nat D'hist Nat 186:567–606

Brown GF, Coleman RG (1972) The tectonic framework of the Arabian Peninsula, 24th Int. Geol Congr Montr 3:300–305

Central Agency for Public Mobilization and Statistics (CAPMAS) of the Arab Republic of Egypt (2014). http://www.capmas.gov.eg/?lang=2. Accessed 04 Dec 2014

Cigna F, Bateson L, Jordan C, Dashwood D (2014) Simulating SAR geometric distortions and predicting Persistent Scatterer densities for ERS-1/2 and ENVISAT C-band SAR and InSAR applications: nationwide feasibility assessment to monitor the landmass of Great Britain with SAR imagery. Remote Sens Environ 152:441–466. doi:10.1016/j.rse.2014.06.025

El-Sayed MM (2003) Neoproterozoic magmatism in NW Sinai, Egypt: magma source and evolution of collision related intracrustal anatectic leucogranite. Int J Earth Sci (Geol Rundsch) 92:145–164. doi:10.1007/s00531-003-0313-3

Eyal M (1975) Stages in the magmatic history of the Precambrian in Sinai and Southern Negev (in Hebrew). PhD Thesis, Hebrew University, Jerusalem

Eyal Y, Eyal M (1987) Mafic dyke swarms in the Arabian–Nubian Shield. Isr J Earth Sci 36:195–211

Fraser DC (1969) Contouring of VLF-EM data. Geophysics 34:958–967. doi:10.1190/1.1440065

Friz-Topfer A (1991) Geochemical characterization of Pan-African dyke swarms in southern Sinai: from continental margin to intraplate magmatism. Precambr Res 49:281–300. doi:10.1016/0301-9268(91)90038-C

Gaber A, Ghoneim E, Khalaf F, El-Baz F (2009) Delineation of paleolakes in the Sinai Peninsula, Egypt, using remote sensing and GIS. J Arid Environ 73(1):127–134. doi:10.1016/j.jaridenv.2008.08.007

Garfunkel Z (1999) History and paleogeography during the Pan-African orogen to stable platform transition: reappraisal of the evidence from Elat area and northern Arabian–Nubian Shield. Israel J Earth Sci 48:135–157

Goddard JV, Evans JP (1995) Chemical-change and fluid-rock interaction in faults of crystalline thrust sheets, Northwestern Wyoming, USA. J Struct Geol 17:533–547. doi:10.1016/0191-8141(94)00068-B

Greiling RO, Abdeen MM, Dardir AA, El Akhal H, El Ramly MF, Kamal GED, Osman AF, Rashwan AA, Sadek MF (1994) A structural synthesis of the Proterozoic Arabian–Nubian Shield in Egypt. Geol Rundsch 83(3):484–501

Gudmundsson A (2000) Active fault zones and groundwater flow. Geophys Res Lett 27(18):2993–2996. doi:10.1029/1999GL011266

Huffman GJ, Adler RF, Bolvin DT, Gu G, Nelkin EJ, Bowman KP, Hong Y, Stocker EF, Wolff DB (2007) The TRMM multi-satellite precipitation analysis: quasi-global, multi-year, combined-sensor precipitation estimates at fine scale. J Hydrometeorol 8:38–55

Iacumin M, Marzoli A, El Metwally AA, Piccirillo EM (1998) Neoproterozoic dyke swarms from southern Sinai (Egypt): geochemistry and petrogenetic aspects. J Afr Earth Sc 26(1):49–64

Issar A, Gilad D (1982) Groundwater flow systems in the arid crystalline province of southern Sinai. J Hydrol Sci 27(3):309–325

Jensen SK, Domingue JO (1988) Extracting topographic structure from digital elevation data for geographic information system analysis. Photogramm Eng Remote Sensing 54(11):1593–1600

Johnson PR, Woldehaimanot B (2003) Development of the Arabian–Nubian Shield: perspectives on accretion and deformation in the northern East African Orogen and the assembly of Gondwana: Geological Society. Lond Spec Publ 206:289–325. doi:10.1144/GSL.SP.2003.206.01.15

Klein J, Lajoie J (1980) Electromagnetic prospecting for minerals. Practical geophysics for the exploration geologists. Northwest Mining Association, Spokane, pp 239–290

Klitzsch E, List FK, Pohlmann G (1987) Geological map of Egypt. Conoco Coral and Egyptian General Petroleum Company, Cairo

Kummerow C, Barnes W, Kozu T, Shiue J, Simpson J (1998) The tropical rainfall measuring mission (TRMM) sensor package. J Atmos Ocean Technol 15:809–816

Kusky TM, El-Baz F, Morency JR, El-Shafei M (1998) Structural and tectonic features of the Sinai Peninsula, using Landsat data: implications for groundwater exploration. Egypt J Remote Sens Space Sci 1:69–100

Lu Z, Meyer DJ (2002) Study of high SAR backscattering caused by an increase of soil moisture over a sparsely vegetated area: implications for characteristics of backscattering. Int J Remote Sens 23(6):1063–1074

Martz W, Garbrecht J (2002) Channel network delineation and watershed segmentation in the TOPAZ digital landscape analysis system. In: Lyon GJ (ed) GIS for water resources and watershed management. Taylor & Francis Inc, London, pp 7–16. doi:10.1201/9780203217917.ch1

Meneisy M (1990) Vulcanicity. In: Said R (ed) The geology of Egypt. Balkema, Rotterdam, pp 157–172

Moore JM (1979) Tectonics of the Najd transcurrent fault system, Saudi Arabia. J Geol Soc 136(4):441–452. doi:10.1144/gsjgs.136.4.0441

Moustafa AR (1997) Controls on the development and evolution of transfer zones: the influence of basement structure and sedimentary thickness in the Suez rift and Red Sea. J Struct Geol 19(6):755–768. doi:10.1016/S0191-8141(97)00007-2

Moustafa AR, Khalil MH (1994) Structural characteristics and tectonic evolution of north Sinai fold belts. In: Said R (ed) The geology of Egypt. A.A. Balkema, Rotterdam, pp 381–389

Moustafa AR, Salama ME, Khalil SM, Fouda HGA (2013) Sinai hinge belt: a major crustal boundary in NE Africa. J Geol Soc 171(2):239–254. doi:10.1144/jgs2013-021

Notti D, Garcia-Davallilo JC, Herrera G, Mora O (2010) Assessment of the performance of Xband satellite radar data for landslide mapping and monitoring: upper Tena valley case study. Nat Hazards Earth Syst Sci 10:1865–1875. doi:10.5194/nhess-10-1865-2010

Notti D, Meisina C, Zucca F, Colombo A (2011) Models to predict Persistent Scatterers data distribution and their capacity to register movement along the slope. In Fringe workshop, 19–23 September 2011. ESA/ESRIN Frascati, Italy

Palacky GJ, Ritsema IL, Dejong SJ (1981) Electromagnetic prospecting for groundwater in Precambrian Terrains in the Republic of Upper Volta. Geophys Prospect 29:932–955. doi:10.1111/j.1365-2478.1981.tb01036.x

Paterson NR, Ronka V (1971) Five years of surveying with very low frequency—electromagnetic method. GeoExplorer 9:7–26. doi:10.1016/0016-7142(71)90085-8

Rosenthal E, Zilberbrand M, Livshitz Y (2007) The hydrochemical evolution of brackish groundwater in central and northern Sinai (Egypt) and in the western Negev (Israel). J Hydrol 337:294–314. doi:10.1016/j.jhydrol.2007.01.042

Shalaby A (2010) The northern dome of Wadi Hafafit culmination, Eastern Desert, Egypt: structural setting in tectonic framework of a scissor-like wrench corridor. J Afr Earth Sc 57(3):227–241. doi:10.1016/j.jafrearsci.2009.08.003

Shendi E, Abouelmagd A (2004) New approach for ground geophysics in the development of groundwater in the basement terrains (A case study from South Sinai, Egypt). In: Proceedings of the 7th conference Geology of Sinai for Development, Ismailia, Egypt, pp 129–140

Shimron AE (1973) The Precambrian structural and metamorphic history of the Eilat Area with comparative notes of the Sinai Peninsula. PhD Thesis, Hebrew University, Jerusalem

Shoshany M, Svoray T, Curran P, Foody M, Perevolotsky A (2000) The relationship between ERS-2 SAR backscatter and soil moisture: generalization from a humid to semi-arid transect. Int J Remote Sens 21(11):2337–2343

Stern RJ, Gottfried D, Hedge CE (1984) Late Precambrian rifting and crustal evolution in the northeast Desert of Egypt. Geology 12:168–172. doi:10.1130/0091-7613(1984)12<168:LPRACE>2.0.CO;2

Stern RJ, Sellers G, Gottfried D (1988) Bimodal dyke swarms in the North Eastern Desert of Egypt: significance for the origin of late Precambrian "A-type" granites in northern Afro-Arabia. In: El Gaby S, Greiling RO (eds) The Pan-African belt of Northeast Africa and adjacent areas. Vieweg, Weisbaden, pp 147–177

Sultan M, Arvidson RE, Sturchio NC, Guinness EA (1987) Lithologic mapping in arid regions with Landsat Thematic Mapper data. Meatiq Dome, Egypt. Geol Soc Am Bull 99:748–762. doi:10.1130/0016-7606(1987)99<748:LMIARW>2.0.CO;2

Sultan M, Arvidson RE, Duncan IJ, Stern RJ, El Kaliouby B (1988) Extension of the Najd shear system from Saudi Arabia to the central Eastern Desert of Egypt based on integrated field and Landsat observations. Tectonics 7(6):1291–1306. doi:10.1029/TC007i006p01291

Sultan M, Becker R, Arvidson RE, Shore P, Stern RJ, El Alfy Z, Guinness EA (1992) Nature of the Red Sea crust: a controversy revisited. Geology 20(7):593–596. doi:10.1130/00917613(1992)020<0593:NOTRSC>2.3.CO;2

Sultan M, Becker R, Arvidson RE, Shore P, Stern RJ, El Alfy Z, Attia RI (1993) New constraints on Red Sea rifting from correlations of Arabian and Nubian Neoproterozoic outcrops. Tectonics 12(6):1303–1319. doi:10.1029/93TC00819

Sultan M, Sturchio N, Hassan FA, Hamdan MAR, Mahmood AM, ElAlfy Z, Stein T (1997) Precipitation source inferred from stable isotopic composition of Pleistocene groundwater and carbonate deposits in the Western Desert of Egypt. Quatern Res 48:29–37. doi:10.1006/qres.1997.1907

Sultan M, Yan E, Sturchio N, Wagdy A, Abdel Gelil K, Manocha N, Becker R, Milewski A (2007) Natural discharge: a key to sustainable utilization of fossil groundwater. J Hydrol 335:25–36. doi:10.1016/j.jhydrol.2006.10.034

Sultan M, Wagdy A, Manocha N, Sauck W, Abdel Gelil K, Youssef AF, Becker R, Milewski A, El Alfy Z, Jones C (2008) An integrated approach for identifying aquifers in transcurrent fault systems: the Najd shear system of the Arabian Nubian shield. J Hydrol 349:475–488. doi:10.1016/j.jhydrol.2007.11.029

Sultan M, Yousef AF, Metwally S, Becker R, Milewski A, Sauck W, Sturchio N, Mohamed A, Wagdy A, El Alfy Z, Becker D, Sagintayev Z, El Sayed M, Welton B (2011) Red sea rifting controls on aquifer distribution: constraints from geochemical, geophysical, and remote sensing data. Geol Soc Am Bull 123:911–924. doi:10.1130/B30146.1

Sultan YM, Abu Alam T, Stuwe K (2012) Tectonic setting of south Sinai metamorphic belts. Geophysical research abstracts, EGU general assembly 14, EGU2012-8344, Vienna, Austria

Telford WM, Geldart LP, Sheriff RE (1990) Applied geophysics. Cambridge University Press, Cambridge, pp 62–134

Thorweihe U (1982) Hydrogeologie des Dakhla-Beckens (Ägypten) [Hydrogeology of the Dakhla Basin (Egypt)]. Berl Geowiss Abh (A) 38:1–53

Toth J (2009) Gravitational systems of groundwater flow—theory, evaluation, utilization. Cambridge University Press, Cambridge, p 297

Wagner W, Scipal K (2000) Large-scale soil moisture mapping in Western Africa using the ERS scatterometer. IEEE Trans Geosci Remote Sens 38:1777–1782

Wang C, Qi J, Moran S, Marsett R (2004) Soil moisture estimation in a semiarid rangeland using ERS-2 and TM imagery. Remote Sens Environ 90:178–189. doi:10.1016/j.rse.2003.12.001

Wang SG, Li X, Han J, Jin R (2011) Estimation of surface soil moisture and roughness from multi-angular ASAR imagery in the watershed allied telemetry experimental research (WATER). Hydrol Earth Syst Sci 15:1415–1426. doi:10.5194/hess-15-1415-2011

Wickel AJ, Jackson TJ, Wood EF (2001) Multitemporal monitoring of soil moisture with RADARSAT SAR during the 1997 Southern Great Plains hydrology experiment. Int J Remote Sens 22:1571–1583

Younes AI, McClay K (2002) Development of accommodation zones in the Gulf of Suez—Red Sea rift, Egypt. AAPG Bull 86(6):1003–1026. doi:10.1306/61EEDC10-173E-11D7-8645000102C1865D